Chalcogenide Letters

Tech Science Press

http://doi.org/10.32604/cl.2026.076592

ARTICLE

Mechanically Stable, Thermodynamic, Photo-Catalytic and Ferromagnetic Characteristic of Ferrites $Al_2Mn(S/Se)_4$ for Energy Storage Applications: DFT-Calculations

Hosam O. Elansary[1], Naveed A. Noor[2], Syed M. Ahmad[3], Humza Riaz[3] and Sohail Mumtaz[4,*]

[1]Prince Sultan Bin Abdulaziz International Prize for Water Chair, Prince Sultan Institute for Environmental, Water and Desert Research, King Saud University, Riyadh 11451, Saudi Arabia
[2]Department of Physics, University of Sargodha, Sargodha, 40100, Pakistan
[3]Department of Physics, University of Lahore, Lahore, 54590, Pakistan
[4]Department of Chemical and Biological Engineering, Gachon University, 1342 Seongnamdaero, Sujeong-gu, Seongnam-si, 13120, Republic of Korea
*Corresponding Author: Sohail Mumtaz. Email: sohail38@gachon.ac.kr

Received: 29 September 2025; Accepted: 23 November 2025; Published: 26 January 2026

ABSTRACT: Ferrites are remarkable compounds for energy harvesting and spintronic applications. For this purpose, mechanically stable, thermodynamic, photo-catalytic, and ferromagnetic characteristics of ferrites $Al_2Mn(S/Se)_4$ have been investigated significantly using PBEsol-GGA and modified Becke Johnson potential (TB-mBJ). In order to determine structural stability, we calculate formation energy (E_f) and Born stability criteria that confirm the structural stability of the $Al_2Mn(S/Se)_4$. 2D and 3D plots of Poisson's ratio (υ) and linear compressibility are also used to indicate the stability of these materials. Additionally, thermodynamic characteristics reveal that both ferrites are stable. Spin-polarized electronic properties indicate that both ferrites are ferromagnetic semiconductors with bandgap values of 2.0 eV and 1.3 eV. The hybridization process, exchange constants, double exchange mechanism, and exchange energies are useful in ferromagnetism. The ferromagnetism has been produced due to exchange of spin of electrons rather than the clustering effects of the interior magnetic field of Mn atoms in the structures. It was confirmed through the decrease of magnetic moments of M and its movement towards nonmagnetic (Al, S/Se) sites. Finally, photo-catalytic properties are investigated to show appropriate choice for the oxidation of H_2O at pH values 0–7.

KEYWORDS: Ferrites; DFT-calculations; thermodynamic properties; ferromagnetism; elastic constant; photo-catalytic properties

1 Introduction

Ferrites usually have wide optical and electronic bandgaps. Additionally, ferrites offer the ability to engineer bandgap and other optical and electronic properties through doping or substitution [1,2]. Ferrites have been studied as potential candidates for a number of applications, such as solar cells [3], LEDs [4], electroluminescence, and electro-photocatalysis [5], laser diodes [6]. Particular thermoelectric and transport properties along with their optoelectronic properties, make ferrites remarkable. Many spinel compounds possess a large Seebeck coefficient, low thermal conductivity, and high electrical conductivity, making these compounds attractive for thermoelectrics [7]. Chalcogenide-based compounds are the most explored spinels. Thermodynamic and mechanical stability of these spinels are essential requirements

for device manufacturing. For this, different compounds such as spinels, perovskites, double perovskites, transition metal oxides, heusler alloys, and dilute magnetic semiconductors have exclusively been studied for spintronic purposes over the last few years [8–10]. The prime focus of the researcher is the ferromagnetic semiconducting nature of A_2BX_4 ferrites with high Curie temperature [11].

The exchange mechanism can overcome the magnetic frustration due to the geometrical distortion of these compounds [12–15]. The combination of semiconducting and magnetic behavior of such compounds, due to their technological use in spintronic is essential. A ferromagnetic behavior of the magnesium chalcogenides $MgCr_2(S/Se)_4$ was found due to negative magneto-resistive. This is seen as Curie temperature of the same magnesium chalcogenides [16]. The observed temperature for $CdCr_2Se_4$ and $CdCr_2S_4$ as 84.5 K and 129.5 K, respectively [17]. The higher voltage Cr^{3+}/Cr^{4+} couple, Mg-based thiospinel, $MgCr_2S_4$, was studied by Wustrow et al. [18]. Thus, the divalent Mg ion and higher voltage coupling effects minimized the rate of diffusion barrier, asserting to some yielding anionic lattice system [19]. In addition, the interpolation of Mg ion was further observed at various temperature as reported by Long et al. [20] with Ti-based thio-spinels and is suitable for electrochemical recycling. The ferromagnetic spinels with the Colossal Magnetoresistance, introduced as an interesting platform for the researchers in the field of ferromagnetism [21,22]. The large magnetic moments and entire spin polarization of Cr and Mn, $MgMn_2S_4$ and $MgCr_2S_4$ have been observed as best ferro-magnets [23,24]. Further, thermoelectric and magnetic features of $MgPr_2(S/Se)_2$ through DFT-oriented analyses have been reported for spintronic applications [25]. However, there are very limited studies on ferrites $Al_2Mn(S/Se)_4$ on physical characteristics. We explored elastic, ferromagnetic, thermodynamic, photo-catalytic, and electronic structure features of both ferrites in this research work. The prime findings of the research are entire spin polarization with no clusters of Mn and ferromagnetism due to the exchange mechanism.

2 Research Methodology

The compounds under discussion have been investigated through the most accurate and versatile DFT based WIEN2k code [26]. For exploring the electronic structures of the compounds, the FP-LAPW technique was brought into use along with PBEsol approximations. In addition, modified Becke and Johnson (TB-mBJ) potential was also utilized for other physical features along with electronic characteristics [27]. This approach is believed to be the best one in order to explore the Band Gaps of inorganic compounds. Similarly, for the exposure of band gaps and electronic structures of the atoms containing huge atomic numbers, the version two of TB-mBJ is also suitable. The elastic characteristics have been investigated with the help of EiaTools [28]. Some fundamental inputs are necessary in DFT analysis to execute the software. So, the solution of density was further analyzed into plane wave in the interstitial region and spherical harmonic in the muffin-tin region. The cut of values of muffin-tin radius and wave vectors have been set as $R_{MT} \times K_{max} = 8$. The angular momentum allowed the optimal values $\ell_{max} = 10$, whereas the value of Gussain factor remained $G_{max} = 18$. The k-mesh order is set through iteration process the best order to which was $12 \times 12 \times 12$. The conversion or exchange of energy was obtained up to 10^{-3} Ry by the same k-mesh order.

3 Results and Discussion

3.1 Structural Properties

Fig. 1 shows the cubic crystal structures of ferrites $Al_2Mn(S/Se)_4$ having space group 227_*Fd*-3*m*. There are 56 atoms in cubic unit cell wherein FCC lattice was formed by 32 atoms of S/Se occupying the octahedrons and tetrahedrons of Mn and Al atoms. Each corner of the octahedral shared (1/2) to 16 atoms of Mn, while the same of the tetrahedrons shared (1/8) to 8 atoms of Al. The atomic coordination S/Se

(1/4, 1/4, 1/4), Fe (1/2, 1/2, 1/2), and Al (1/8, 1/8, 1/8) have been employed quite in line with the mentioned space group.

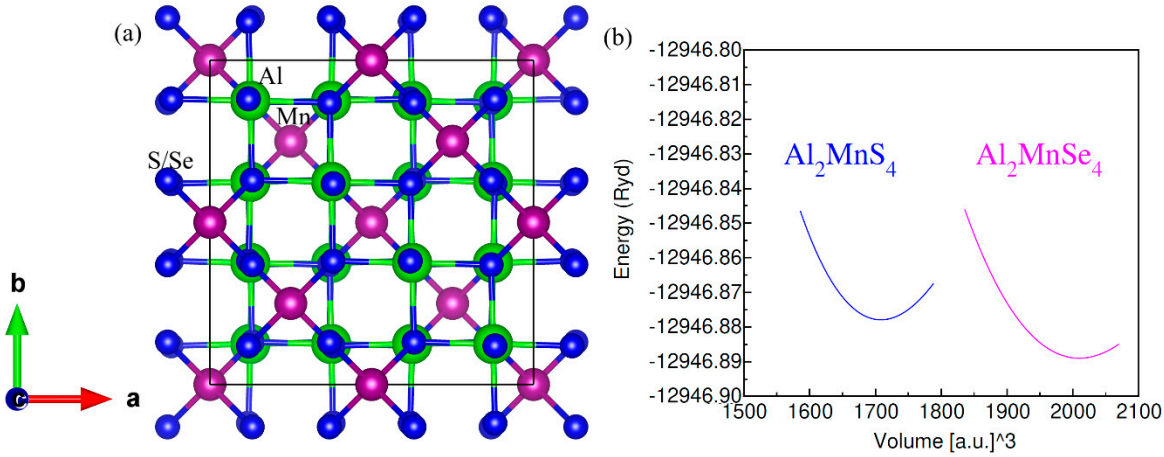

Figure 1: (**a**) ferro-magentic unit cell and (**b**) optimization plot of ferrites $Al_2Mn(S/Se)_4$.

The lattice parameters and bulk modulus of ferrites $Al_2Mn(S/Se)_4$ were evaluated by setting Equation of State [29] to volume data versus total energy. Table 1 exhibits the computed values for structural features. The increase in anionic radii up to 1.840 Å from 1.700 Å for Se and S correspondingly caused an increase in lattice parameter up to 10.04 Å from 10.60 Å. On the other hand, smaller electro-negativity and bigger atomic radius of selenium is perceived from the reduction in covalent character between anions and cations. Similarly, increase in bulk modulus caused reduction in stiffness from Al_2MnS_4 to Al_2MnSe_4.

Table 1: The computed lattice parameter, bulk modulus values and formation energy of ferrites $Al_2Mn(S/Se)_4$.

Ferrites	a_o (Å)	B_o (GPa)	ΔH_f
Al_2MnS_4	10.04	90.49	−0.94
Al_2MnSe_4	10.60	69.81	−0.68

Both ferrites $Al_2Mn(S/Se)_4$ reportedly possess more stability than that of other Mn-based compounds. The formation energy is computed by the equation as under:

$$\Delta H_f = E_{Total}(Al_l Mn_m S/Se_n) - lE_{Al} - mE_{Mn} - nE_{S/Se} \quad (1)$$

where $E_{Total}(Al_l Mn_m S/Se_n)$ is the total energy, (E_{Mn}, E_{Al} and $E_{S/Se}$) are the amounts energy levels of (Al, mn, and S/Se) atoms. The computed figures of ΔH_f in Table 1 displaying the negative sign confirms that the compounds are thermodynamically stabile in FM states [30,31].

3.2 Mechanical Properties

Mechanical analysis requires three independent elastic constants computed for the studied ferrites $Al_2Mn(S/Se)_4$. Charpin method is used to set a criterion for mechanical stability [32,33]. It is ensured that our examined DPs are mechanically stable from the Reuss-Voigt approximations and other criteria for stability [34]. Furthermore, the relation $B = C_{11} + 2C_{12}/2$ is used to compute bulk modulus from elastic constants. Calculations done for Young, shear moduli (E, G), Pugh's ratio B/G, anisotropy factor (A) and Poisson's ratio (υ), elaborate the mechanical character of the material given in Table 1. The examined DPs

have the malleable character due to relatively small moduli (B, Y, G). Pugh's (B/G) ratio determines the ductility and brittleness nature of a crystal. It is observed that compounds under investigation retain their ductile nature regardless of the pressure exerted [35]. The B/G > 1.75 confirms the ductility of the studied compound. In our studied ferrites $Al_2Mn(S/Se)_4$ the ferrite Al_2MnS_4 has greater ductility while ferrite Al_2MnSe_4 reveals lesser ductility. The directional response of the studied ferrites are determined by the anisotropic factor A. It demonstrates the changing physical behavior along particular axis. The material is isotopic when A = 0 but when it deviates the material's character becomes anisotropic. Our studied ferrites explicitly show anisotropic behavior. The nature of the bonding of the material is revealed by the Poisson ratio (υ), ionic bonding is observed when υ = 0.26, υ < 0.26 reveals covalent nature while υ > 0.26 is for metallic nature of bonding. Covalent nature of bonding is observed in all atmospheric conditions for the DPs under examination as the value for Poisson ratio remains greater than 0.26. Moreover, Poisson ratio also determines the ductility υ > 0.26 and brittleness υ < 0.26 [36], ductility of our compound is further testified by its value.

To investigate elastic anisotropy, three-dimensional surface plots (see Figs. 2 and 3) of bulk modulus (B), shear modulus (G), Young's modulus (Y), Pugh (B/G) and Poisson's ratio (υ) were created. The bulk modulus is almost spherical, confirming its isotropic nature.

However, G, Y, and ν show considerable departures from spherical geometry, indicating elastic anisotropy in both ferrites. This anisotropy is further demonstrated by the variations in minimum and maximum G and Y values, which show the directional dependence of mechanical reaction. The estimated elastic constants, moduli, and anisotropy analysis reveal that ferrites $Al_2Mn(S/Se)_4$ are mechanically stable, ductile material with noticeable elastic anisotropy, making it an attractive candidate for possible applications in energy-related and optoelectronic devices.

3.3 Thermodynamic Properties

One of the main thermodynamic parameters that is frequently studied in proteins is heat capacity (C). It is the most difficult of these quantities to comprehend physically, yet it offers the most knowledge, with over six definitions [37]. Fig. 4a shows that heat capacity at constant pressure (C_p) increases rapidly at low temperatures and then starts to level off. Among the three compounds, ferrites Al_2MnSe_4 (green) has the highest heat capacity, followed by Al_2MnS_4 (black). This pattern most likely reflects the chalcogenide rising atomic mass (S < Se), which influences vibrational modes and, consequently, heat capacity. Heat capacity at constant volume (C_V) can provide information about solid phase transition, energy band structure, lattice vibration, etc. [38]. The C_V calculation result is displayed in Fig. 4b. At temperatures below 200 K, C_V rises quickly but for temperatures greater than 200 K there is very small increase in it. From 400 K it tends to be a constant, reaching a maximum of 241 J/kg·K. Consequently, C_V for S is more than Se for all temperatures. Since materials experience energy conversion and dissipation during the operation, so it is important to understand their thermal behaviour. The product of entropy (S) and temperature (T), i.e., S × T, enthalpy (H), and free energy (F) variations with temperature are depicted in Fig. 4c. The thermodynamic potentials given as enthalpy H = U + PV and Helmholtz free energy F = U − TS, where U, P, and V stand for the system's internal energy, pressure, and volume, respectively. Fig. 4c shows that T*Enthalpy increases, while there is very small rise in enthalpy with increase in temperature. But Free energy decreases with temperature rise, indicating thermodynamic stability at higher temperatures. Al_2MnSe_4 (green) consistently has the highest T*S and enthalpy, but also the most negative free energy, implying better thermal stability. Enthalpy rises as a result of the system's thermal motion being intensified by temperature increases, which also raise

internal energy, pressure, and volume. F = U − TS < U + PV − TS = H − TS, F < H − TS < 0 since H < TS and the three materials' enhanced range of H is less than TS.

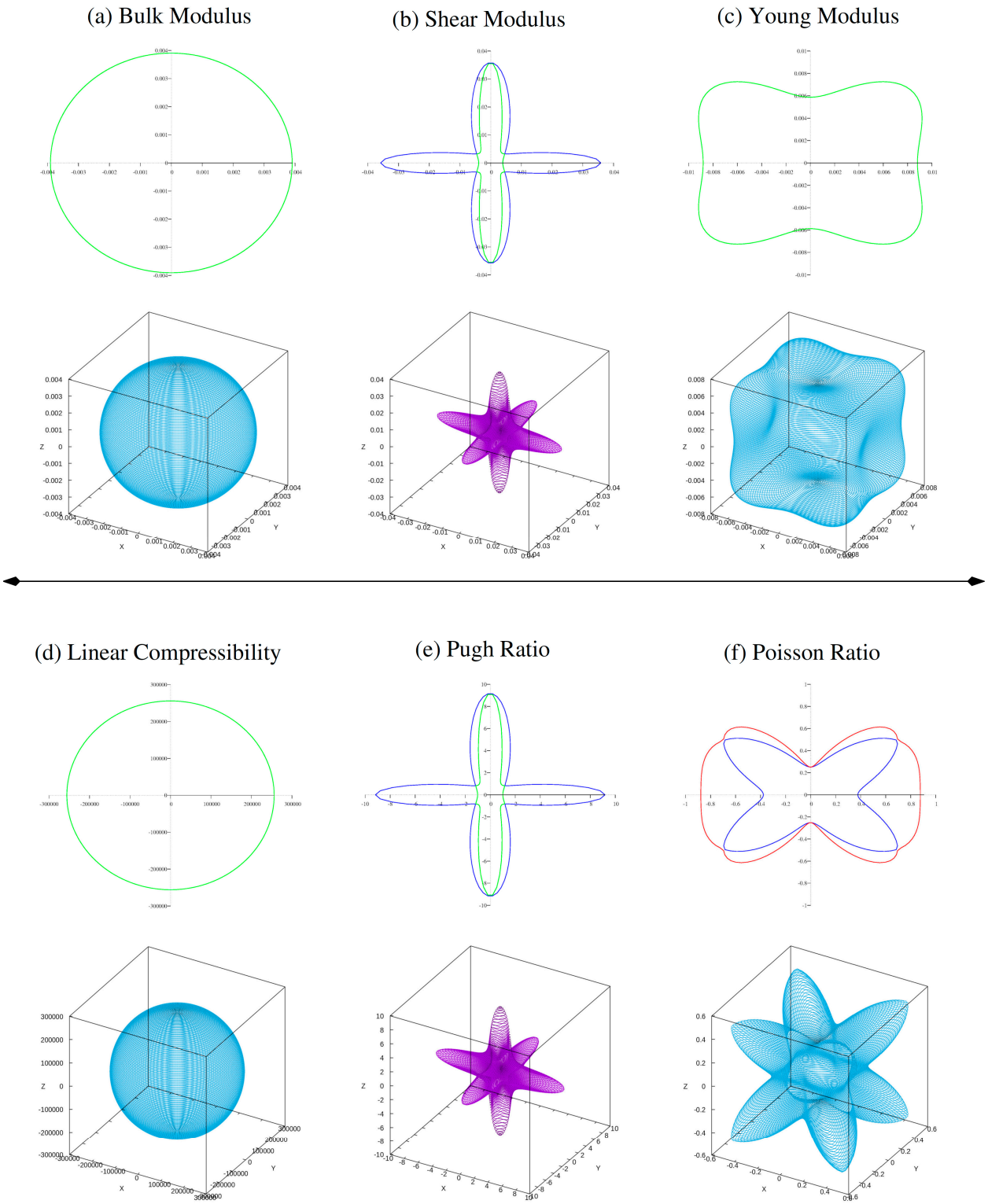

Figure 2: Calculated 2D and 3D plots of (**a**) bulk modulus, (**b**) shear modulus, (**c**) young modulus, (**d**) linear compressibility, (**e**) Pugh ratio and **(f)** Possion ratio of ferrite Al_2MnS_4.

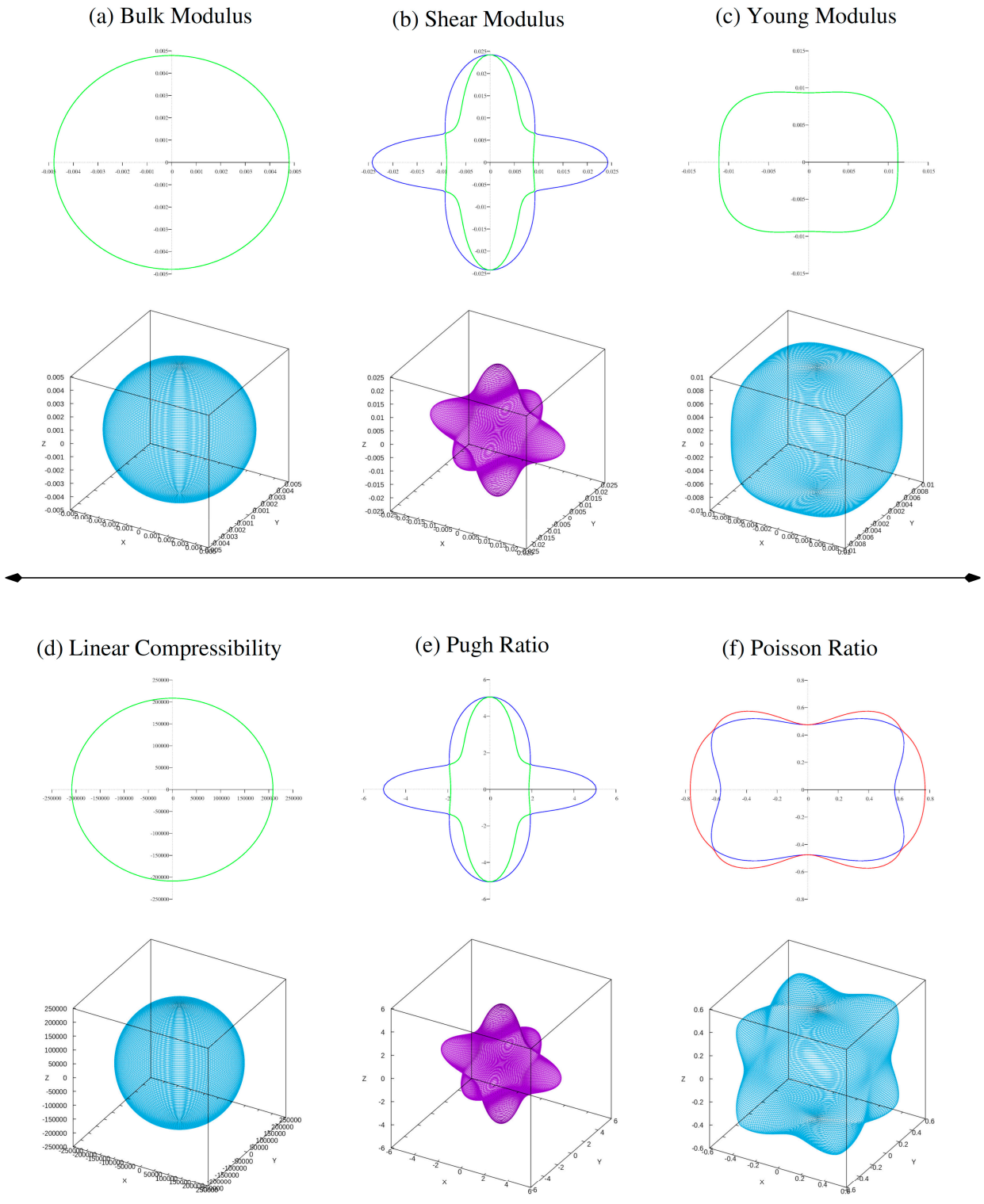

Figure 3: Calculated 2D and 3D plots of (**a**) bulk modulus, (**b**) shear modulus, (**c**) young modulus, (**d**) linear compressibility, (**e**) Pugh ratio and (**f**) Possion ratio of ferrite Al_2MnSe_4.

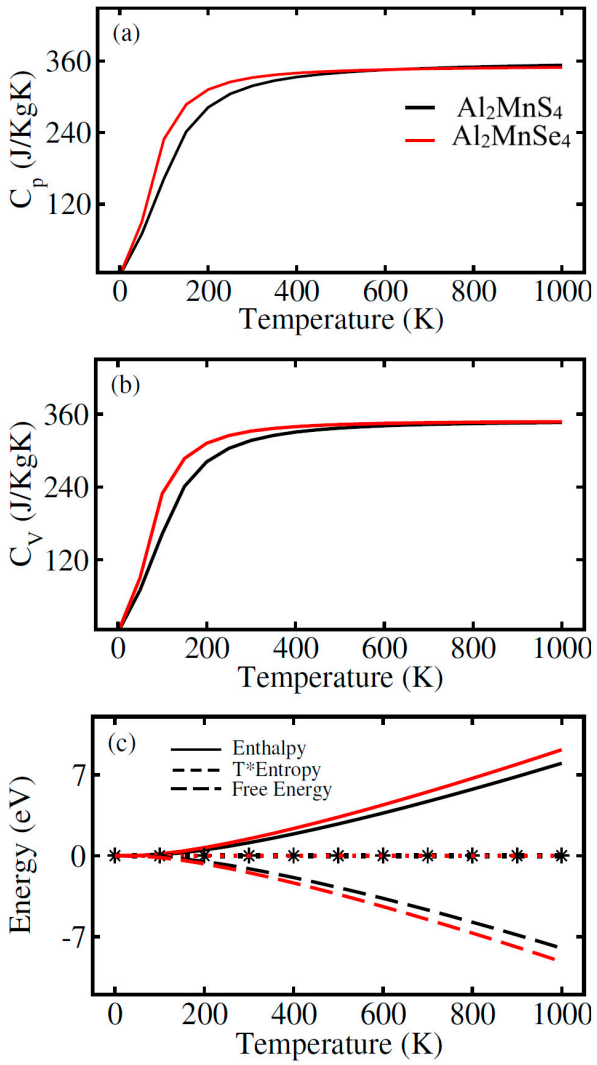

Figure 4: Calculated thermodynamic properties of ferrites $Al_2Mn(S/Se)_4$. (**a**) heat capacity of at constant pressure vs. temperature (Cp); (**b**) heat capacity of at constant volume (Cv) vs. temperature; (**c**) T*entropy vs. temperature, enthalpy vs. temperature, free energy vs. temperature.

3.4 Ferro-Magnetic Properties

In electronic properties, spin polarized analysis of electronic band structure are investigated for ferromagnetic behavior of studied ferrites $Al_2Mn(S/Se)_4$. In spin-polarized electronic band calculations, we used TB-mBJ potential for the accurate calculations of bandgap of both ferrites $Al_2Mn(S/Se)_4$ that depict in Fig. 5a,b. In Fig. 5, the horizontal dotted lines between valence band (VB) and conduction band (CB) show the Fermi level. In both spin channels, CB minima and VB maxima convene at Γ point. Thus, the both ferrites are justified to exhibit direct bandgap having calculated values of 2.0 eV and 1.3 eV respectively. The band structure ensures that both channel are semiconductor behavior. The states are away from the E_F in CB minima whereas near the E_F in VB maxima for $Al_2Mn(S/Se)_4$ for minority spin. On contrary, conduction states have been found away the E_F whereas the valence states have been observed existing at the E_F in majority channel forming the narrower bandgap (see in Fig. 5). Resultantly, the BS of the materials can be affected by the change in anions showing its importance and potential [39].

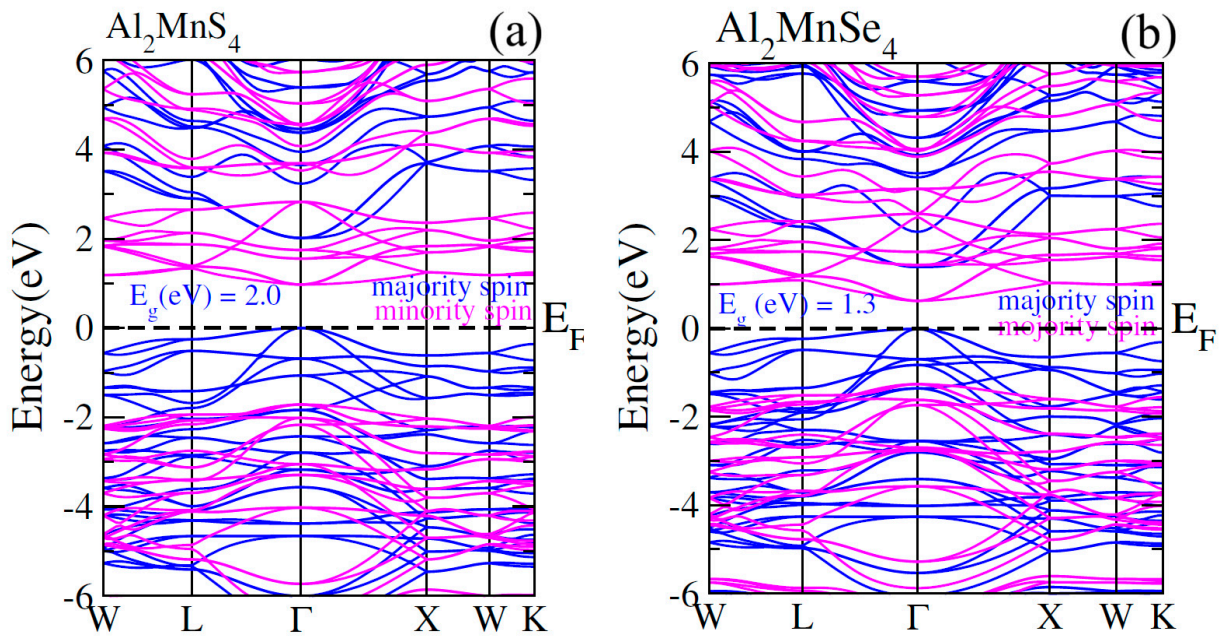

Figure 5: Calculated spin-polarized band structures for (**a**) Al_2MnS_4 and (**b**) Al_2MnSe_4 majority spin and minority spin.

However, in the work in hand, spin down and spin up states have been reverted because of quantum confinement effects where the wave function of electrons remained limited in quantum [40]. Thus, powerful hybridization takes place among S/Se-p and Mn-3d states manipulating the ferromagnetic interaction [41]. 3d-e_g states remained exclusively donated to (↑) channel as compared with (↓) channel in lesser energy region, −3 eV to −1 eV whereas the same states higher energy region remained greatly contributed towards hybridization for Al_2MnS_4. However, the contribution of theirs reduced as anion changing from S to Se. As far as the matter of 3d-t_{2g} states is concerned, the contribution was approximately the same for the both anions. It has been discussed in details in the high energy region 1 eV–3 eV (see Fig. 5).

3.5 Photo-Catalytic Properties

Solar energy can be captured and hydrogen can be produced by dissociating water with the right direct bandgap semiconductors [42]. Thus, clean, sustainable energy can be produced by photocatalytic water splitting [43]. Electrons reduce water during the photocatalytic process, while holes oxidize it [44]. The conduction and valence band photocatalytic water splitting must be greater than the oxidation (reduction) potential of 0 (1.23) eV for this activity for all materials considered [45]. For photocatalytic water splitting, the typical oxidation as well as reduction potentials are −4.44 eV and −5.67 eV, respectively, on the hydrogen scale, as shown in Fig. 6. The Fermi level is set to (−4.44) eV in order to determine the band edge positions of the VB and CB with respect to standard oxidation [46]. At 0 eV = −4.4 eV and 1.23 eV = −5.67 eV, respectively, the CB and VB are positioned. Normal redox potentials can be affected by the pH of the water. One can use the formula to determine the redox potential at various pH values: E H/H_2 = 4.44 eV + pH × 0.059 eV and E O_2/H_2O = 5.67 eV + pH × 0.059 eV. At pH = 0 (typical aqueous acid conditions for redox processes), the standard potential is 4.44 eV for water reduction and 5.67 eV for oxidation. The figure makes it evident that $Al_2Mn(S/Se)_4$ showing for the oxidization of H_2O at pH values 0–7. So ferrites $Al_2Mn(S/Se)_4$ fail to reduction of water from pH = 0–7, but being good response for the oxidization of water.

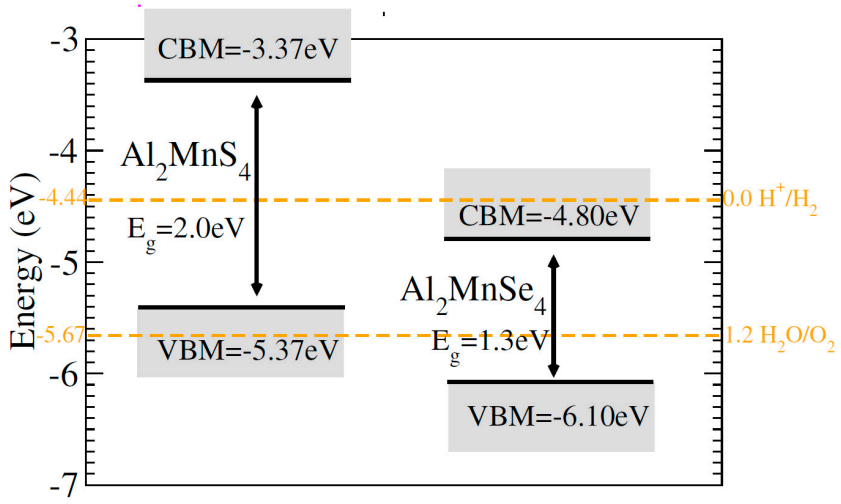

Figure 6: Calculated photo-catalytic properties of ferrites $Al_2Mn(S/Se)_4$.

4 Conclusion

The thermodynamic, mechanical, photo-catalytic, and ferro-magnetic characteristics of ferrites $Al_2Mn(S/Se)_4$ were comprehensively investigated using density functional theory. Both materials have cubic structures with a certain space group. The elastic stiffness constants verified the mechanical stability of materials, and the calculated Pugh and Poisson ratios are observed as 0.27 and 1.76, respectively showing ductility of these materials. Formation energies (ΔHf), measured as −0.94 eV for Al_2MnS_4 and −0.64 eV for Al_2MnSe_4 confirmed the thermodynamic stability. The exothermic reaction with negative magnitude validates the thermodynamic stability. Moreover, the S-based compound was found to be more stable due to larger amplitude of ΔH_f. The direct bandgaps of 2.0 eV and 1.3 eV in up-spin configuration for Al_2MnS_4 and Al_2MnSe_4, respectively, spin-polarized electronic band structure verified the semiconducting properties. Photo-catalytic calculations are evident that ferrites $Al_2Mn(S/Se)_4$ show for the oxidation of H_2O at pH values 0–7.

Acknowledgement: The authors extend their appreciation to the Deanship of Scientific Research, King Saud University for funding through the Vice Deanship of Scientific Research Chairs; Research Chair of Prince Sultan Bin Abdulaziz International Prize for Water.

Funding Statement: This research was funded by the Deanship of Scientific Research, King Saud University through the Vice Deanship of Scientific Research Chairs; Research Chair of Prince Sultan Bin Abdulaziz International Prize for Water.

Author Contributions: Naveed A. Noor: Software, Data curation, Visualization, Supervision, Syed M. Ahmad: Conceptualization, Methodology, Humza Riaz; Investigation, Validation. Sohail Mumtaz: Writing—Original draft preparation and Hosam O. Elansary: Writing—Reviewing and Editing. All authors reviewed and approved the final version of the manuscript.

Availability of Data and Materials: Data available on request from the authors.

Ethics Approval: Not applicable.

Conflicts of Interest: The authors declare no conflicts of interest.

References

1. Hemberger J, Lunkenheimer P, Fichtl R, Krug von Nidda HA, Tsurkan V, Loidl A. Relaxor ferroelectricity and colossal magnetocapacitive coupling in ferromagnetic $CdCr_2S_4$. Nature. 2005;434(7031):364–7. [CrossRef].
2. Ohgushi K, Ogasawara T, Okimoto Y, Miyasaka S, Tokura Y. Gigantic Kerr rotation induced by a *d*–*d* transition resonance in MCr_2S_4 (M = Mn, Fe). Phys Rev B. 2005;72:155114. [CrossRef].
3. Zentefis NP, Fiore A, Yang Y. Recent Advancements of Spinel Oxide Materials in Energy and Fuel Applications. Energy Fuels. 2025;39(15):7167–81. [CrossRef].
4. Prajapati N, Kumar M, Pandey V, Munjal S, Pandey H. White LED-based photocatalytic treatment using recoverable cobalt ferrite nanoparticles. Phys Scr. 2025;100(9):095922. [CrossRef].
5. Pandey SK. Orbital ordering in the geometrically frustrated MgV_2O_4: *ab initio* electronic structure calculations. Phys Rev B. 2011;84:094407. [CrossRef].
6. Jogi JK, Singhal SK, Mishra R, Tanna AR, Jangir R, Singh A, et al. Study of structural and magnetic properties of laser-irradiated zinc ferrite material. Radiat Eff Defects Solids. 2025;180(3-4):447–62. [CrossRef].
7. Anwar A, Noor NA, Mustafa GM, Atiq S, Ibrahim A, Laref A. Mechanically robust and thermodynamically stable FeSc2Z4 (Z = S, Se) spinels for future spintronic architectures. RSC Adv. 2025;15(43):35770–81. [CrossRef].
8. Vinay D, Devaraja C. A comprehensive review of structural, and optical properties of boronated glasses doped with 3-d transition metal oxides (TMOs). J Alloys Compd. 2025;1024:180145. [CrossRef].
9. Khatun N, Chiu CY, Lin CJ, Lin JY, Wang SF, Yang TC. Enhancing the performance of ammonia-fed intermediate temperature solid oxide fuel cells (IT-SOFCs) through the application of Ni2MnGa Heusler alloy on the anode surface. J Power Sources. 2024;600:234252. [CrossRef]
10. Chen X, Wei P, Chen T, Ye X, Ge J, Tang Z, et al. Ferromagnetism enhancing thermoelectric transport properties in dilute magnetic semiconductor $Ge_{1-x}Mn_xTe$. Sci China Mater. 2025;68(8):2841–9. [CrossRef].
11. Reehuis M, Krimmel A, Büttgen N, Loidl A, Prokofiev A. Crystallographic and magnetic structure of ZnV_2O_4. Structural phase transition due to spin-driven Jahn-Teller distortions. Eur Phys J B. 2003;35:311–16. [CrossRef].
12. Das A, Ranaut D, Pal P, Pal R, Moulick S, Das M, et al. Tuning of magnetic frustration and emergence of a magnetostructural transition in $Mn_{1-x}Cd_xCr_2O_4$. Phys Rev B. 2023;108(6):064426. [CrossRef].
13. Rathi A, Babu PD, Sahlot P, Awasthi AM, Chaudhary S, Patnaik S, et al. Interplay of spin and orbital ordering in a frustrated spinel chromite. J Phys Condens Matter. 2023;36(13):135801. [CrossRef].
14. Maqsood S, Javed MA, Mumtaz S, Al-Sadoon MK. Computational study of Cd-based chalcogenide spinels $CdSm_2(S/Se)_4$ for spintronic applications. Chalcogenide Lett. 2024;21(6):449–58. [CrossRef].
15. Sandemann JR, Grønbech TB, Støckler KA, Ye F, Chakoumakos BC, Iversen BB. Direct visualization of magnetic correlations in frustrated spinel $ZnFe_2O_4$. Adv Mater. 2023;35(5):2207152. [CrossRef].
16. Lehmann HW, Harbeke G. Semiconducting and optical properties of ferromagnetic $CdCr_2S_4$ and $CdCr_2Se_4$. J Appl Phys. 1967;38(3):946. [CrossRef].
17. Matsumoto G, Ohbayashi K, Kohn K, Iida S. Magnetic properties of $ZnMn_2S_4$, $ZnMn_2Se_4$ and $ZnMn_2Te_4$. J Phys Soc Jpn. 1966;21(11):2429. [CrossRef].
18. Wustrow A, Key B, Phillips PJ, Sa N, Lipton AS, Klie RF, et al. Synthesis and characterization of MgCr2S4 thiospinel as a potential magnesium cathode. Inorg Chem. 2018;57(14):8634–8. [CrossRef].
19. Akther Hossain AKM, Seki M, Kawai T, Tabata H. Colossal magnetoresistance in spinel type $Zn_{1-x}Ni_xFe_2O_4$. J Appl Phys. 2004;96(2):1273–5. [CrossRef].
20. Long J, Liu Y, He Z, Tan S, Xiong F, Xu H, et al. Redesigning solvation structure toward passivation-free magnesium metal batteries. ACS Nano. 2024;18(23):15239–48. [CrossRef].
21. Yang H, Li S, Wu Y, Bao X, Xiang Z, Xie Y, et al. Advances in flexible magnetosensitive materials and devices for wearable electronics. Adv Mater. 2024;36(37):2311996. [CrossRef].
22. Mahmood Q, Hassan M, Murtaza G, Sajjad M, Laref A, Ul Haq B. The theoretical investigation of electronic, magnetic, and thermoelectric behavior of $LiZ2O_4$ (Z = Mn, Fe, Co, and Ni) by modified becke and Johnson approach. J Supercond Nov Magn. 2019;32(5):1231–9. [CrossRef].
23. Sun X, Bonnick P, Duffort V, Liu M, Rong Z, Persson KA, et al. A high capacity thiospinel cathode for Mg batteries. Energy Environ Sci. 2016;9(7):2273–7. [CrossRef].

24. Das A, Lal DS, Nair AM, Thakur VK, Pullanchiyodan A, Raghavan P. Cathode materials for rechargeable magnesium-ion batteries. In: Advanced technologies for rechargeable batteries. Boca Raton, FL, USA: CRC Press; 2024. p. 51–61. [CrossRef].
25. Mahmood A, Rashid M, Safder K, Waqas IM, Noor NA, Ramay SM, et al. Spin-dependent rare-earth-based $MgPr_2X_4$ (X = S, Se) spinels investigations for spintronic and sustainable energy systems applications. Results Phys. 2021;20:103709. [CrossRef].
26. Blaha P, Schwarz K, Madsen GKH, Kvasnicka D, Luitz J. WIEN2K, an augmented plane wave + local orbitals program for calculating crystal properties. Vienna, Austria: Technische Universität Wien; 2001.
27. Koller D, Tran F, Blaha P. Merits and limits of the modified Becke-*Johnson* exchange potential. Phys Rev B. 2011;83(19):195134. [CrossRef].
28. Madsen GKH, Singh DJ. BoltzTraP. A code for calculating band-structure dependent quantities. Comput Phys Commun. 2006;175(1):67–71. [CrossRef].
29. Murnaghan FD. The compressibility of media under extreme pressures. Proc Natl Acad Sci U S A. 1944;30(9):244–7. [CrossRef].
30. Mustafa GM, Noor NA, Iqbal MW, Sajjad M, Naeem MA, Mahmood Q, et al. Study of optoelectronic and transport properties of $MgLu_2Z_4$ (Z = S, Se) spinels for optoelectronic and energy harvesting applications. Mater Sci Semicond Process. 2021;121:105452. [CrossRef].
31. Noor NA, Nasrullah F, Moussa IM, Mumtaz S. Mechanical, magnetic, and electronic characteristics of Sm-based chalcogenides for spintronics and device applications. Chalcogenide Lett. 2024;21(5):413–21. [CrossRef].
32. Jong UG, Yu CJ, Kye YH. Computational prediction of structural, electronic, and optical properties and phase stability of double perovskites K_2SnX_6 (X = I, Br, Cl). RSC Adv. 2020;10(1):201–9. [CrossRef].
33. Anderson OL. A simplified method for calculating the Debye temperature from elastic constants. J Phys Chem Solids. 1963;24(7):909–17. [CrossRef].
34. Pugh SF. XCII. Relations between the elastic moduli and the plastic properties of polycrystalline pure metals. Lond Edinb Dublin Philos Mag J Sci. 1954;45(367):823–43. [CrossRef].
35. Ji X, Yu Y, Ji J, Long J, Chen J, Liu D. Theoretical studies of the pressure-induced phase transition and elastic properties of BeS. J Alloys Compd. 2015;623:304–10. [CrossRef].
36. Roknuzzaman M, Ostrikov KK, Wang H, Du A, Tesfamichael T. Towards lead-free perovskite photovoltaics and optoelectronics by *ab-initio* simulations. Sci Rep. 2017;7(1):14025. [CrossRef].
37. Prabhu NV, Sharp KA. Heat capacity in proteins. Annu Rev Phys Chem. 2005;56:521–48. [CrossRef].
38. Zanib M, Yasir MA, Noor NA, Mumtaz S, Al-Sadoon MK. *Ab-initio* simulation of ferromagnetic chalcogenide CdCe2X4 (X = S, Se) spinels for optoelectronic applications. Chalcogenide Lett. 2024;21(9):695–705. [CrossRef].
39. Yahi H, Meddour A. First principle investigation of structural, electronic and magnetic properties of cubic $Cd_{0.9375}TM_{0.0625}S$ (TM = Ni, Co and Fe). J Magn Magn Mater. 2017;432:591–6. [CrossRef].
40. Mahmood Q, Ul Haq B, Rashid M, Noor NA, AlFaify S, Laref A. First-principles study of magnetic and thermoelectric properties of $SnFe_2O_4$ and $SnCo_2O_4$ spinels. J Solid State Chem. 2020;286:121279. [CrossRef].
41. Mahmood Q, Rouf SA, Rashid M, Jamil M, Sajjad M, Laref A. Tailoring of bandgap to tune the optical properties of $Ga_{1-x}Al_xY$ (Y = As, Sb) for solar cell applications by density functional theory approach. Z Naturforschung A. 2019;74(12):1131–8. [CrossRef].
42. Osterloh FE. Inorganic materials as catalysts for photochemical splitting of water. Chem Mater. 2008;20(1):35–54. [CrossRef].
43. Hu X, Li G, Yu JC. Design, fabrication, and modification of nanostructured semiconductor materials for environmental and energy applications. Langmuir. 2010;26(5):3031–9. [CrossRef].
44. Artero V, Chavarot-Kerlidou M, Fontecave M. Splitting water with cobalt. Angew Chem Int Ed. 2011;50(32):7238–66. [CrossRef].
45. Kudo A. Photocatalysis and solar hydrogen production. Pure Appl Chem. 2007;79(11):1917–27. [CrossRef].
46. Liu JJ, Fu XL, Chen SF, Zhu YF. Electronic structure and optical properties of Ag_3PO_4 photocatalyst calculated by hybrid density functional method. Appl Phys Lett. 2011;99(19):191903. [CrossRef].